In Operando Study of High-Performance Thermoelectric Materials for Power Generation

Document Version
Accepted author manuscript

OPEN ACCESS

In operando study of high-performance thermoelectric materials for power generation: a case study of β-Zn$_4$Sb$_3$

*Le Thanh Hung[1, *], Duc-The Ngo[1, 2], Li Han[1], Bo Brummerstedt Iversen[3], Hao Yin[4], Nini Pryds[1], and Ngo Van Nong[1, **]*

[1]Department of Energy Conversion and Storage, Technical University of Denmark, DTU Risø Campus, 4000 Roskilde, Denmark
[2]Electron Microscopy Centre, School of Materials, University of Manchester, Manchester M13 9PL, United Kingdom
[3]Centre for Materials Crystallography, Department of Chemistry and iNANO, Aarhus University, 8000, Aarhus C, Denmark
[4]TEGnology ApS, Lundagervej 102, 8722, Hedensted, Denmark
*E-mail: lthh@dtu.dk; leehungh@gmail.com
**Email: ngno@dtu.dk
Keywords: Operando study; In-situ thermoelectric; thermoelectric stability; Zn-Sb; thermoelectric application

To date, many high-performance thermoelectric (TE) materials for power generation have been studied and reported. However, so far they have not been implemented in reliable commercial devices. To bring current achievements into a device for power generation, a full understanding the dynamic behavior of thermoelectric materials under operating conditions is needed. In this work, an in operando study is conducted on the high-performance TE material β-Zn$_4$Sb$_3$ under large temperature gradient and thermal cycling by a new approach using *in-situ* transmission electron microscopy combined with characterization of the TE properties. We found that after 30 thermal cycles in a low-pressure helium atmosphere the TE performance of β-Zn$_4$Sb$_3$ is maintained with the *zT* value of 1.4 at 718 K. Nevertheless, under a temperature gradient of 380 K (T$_{hot}$ = 673 K and T$_{cold}$ = 293 K) operating for only 30 hours, zinc whiskers gradually precipitate on the cold side of the β-Zn$_4$Sb$_3$ leg. The dynamical evolution of Zn in the matrix of β-Zn$_4$Sb$_3$ was found to be the source that leads to a high *zT* value by lowering of the thermal conductivity and electrical resistivity, but it is also the failure mechanism for the leg under these conditions. The in operando study brings deep

insight into the dynamic behavior of nanostructured TE materials for tailoring future TE materials and devices with higher efficiency and longer durability.
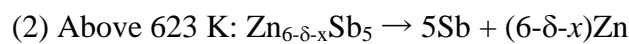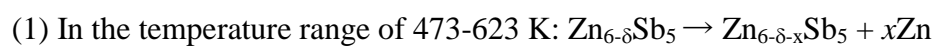
1. Introduction

Thermoelectric power generators (TEGs) can recuperate waste heat by directly converting it into electricity. Due to their advantages, i.e. no moving part, no emission, and limited maintenance, TEGs have gained much attention as one of the most promising renewable energy technologies [1]. To obtain a high conversion efficiency, the materials used to construct a TEG must possess a high value of the dimensionless figure-of-merit, zT, $(z = \alpha\sigma/(\kappa_e+\kappa_L))$, where α, σ, κ_e, and κ_L are the Seebeck coefficient, the electrical conductivity, and the electronic and the lattice components of thermal conductivity, respectively). Hence, to improve the TE performance, an effective approach is to reduce the thermal conductivity without deteriorating the electrical conductivity through e.g. nanostructuring or forming a complex structure. In this context, the "'phonon-glass, electron-crystal" (PGEC) concept proposed by Glen Slack in 1995 [2] has been applied as the key approach to improve the performance of TE materials. In such PGEC "like" materials, the structure allows charge carriers to "pass" the crystal while heat transfer is blocked as in a glass.

The development of TE materials has made an impressive progress [1,3,4] with the high values of zT achieved in many materials such as $zT = 2.6$ at 923 K for tin selenide [5], $zT = 1.5$ at 1200 K for half Heusler alloy [6], $zT = 1.8$ at 823 K for filled Skutterudites [7], $zT = 2.2$ at 915 K [8], and polycrystalline PbTe, $zT = 1.5$ at 1000 K for Cu_2Se [9]. Among the high-performance PGEC materials with a zT above 1 at a moderate temperature range (400–750 K), the Zn_4Sb_3 compound has gained special attention due to its low cost, abundant elements, and environmentally friendly processing [1,10–12].

Zn_4Sb_3 with precise formula composition of $Zn_{13}Sb_{10}$ has a hexagonal rhombohedral crystal structure in space group $R\bar{3}c$ [1,13,14]. In this structure, there are 18 Sb^{3-} and 12 Sb^{2-} ions per

unit cell and a total of 78 negative charges. To balance the electric charge, 39 Zn^{2+} are required, but only 36 sites are available. Therefore, 3 interstitial sites are filled to accommodate the zinc ions [1,15]. The interest in TE Zn_4Sb_3 has gained a momentum since the discovery of high zT value of 1.3 at 670 K was obtained by Caillat et al. in 1996 [11]. This high zT value resulted from an extraordinary low thermal conductivity, which is explained by the concept of PGEC [1,2]. The existence of interstitial Zn atoms and the local structure distortion are attributed to be the main reason for this extraordinary phenomenon [16–19]. Over the years, extended studies have been carried out to improve zT value by various methods including doping/substituting, nano-inclusions, and nanostruturing [20].

Besides increasing the zT, many studies have also been conducted to investigate the thermal stability of this material [11,21–26]. Caillat et al. have shown that TE properties of Zn_4Sb_3 are stable up to 670 K under argon and static vacuum, but unstable in the dynamic vacuum due to the evaporation of Sb at temperatures higher than 543 K resulting in an increased electrical resistivity[11]. Mozharivskyj et al.[14] have observed that the Seebeck coefficient increased at an elevated temperature in a dynamic vacuum (10^{-7} Torr) due to Zn sublimation. The study revealed that Zn sublimates owing to the following two reactions:

(1) In the temperature range of 473-623 K: $Zn_{6-\delta}Sb_5 \rightarrow Zn_{6-\delta-x}Sb_5 + xZn$

(2) Above 623 K: $Zn_{6-\delta-x}Sb_5 \rightarrow 5Sb + (6-\delta-x)Zn$

Here, $Zn_{6-\delta}Sb_5$ is the (assumed) X-ray formula of Zn_4Sb_3 [13,14]. The decomposition of the Zn_4Sb_3 phase has been studied quantitatively using synchrotron powder X-ray diffraction (PXRD) [22–26] as well as by extensive evaluation of physical properties [27,28]. Attempts have also been made to substitute the Zn-sites with various elements such as Mg [22], Cd [23,24,29], and Pb[25]. The results showed that these doped samples are more stable than the non-doped sample under thermal cycling and during heat treatment. With the purpose of blocking the Zn diffusion inside Zn_4Sb_3, nano-sized ZnO and TiO_2 ceramic inclusions have also been

investigated [26]. The TiO$_2$ nanocomposite sample showed significant improvement in thermal stability by retaining 98.8 wt% of the original phase after heating to 625 K, compared with 42 wt% degradation in the pure sample [26]. Although remarkable results have been obtained both respect to the TE performance and the thermal stability at high temperatures, there is virtually no report on the practical use of Zn$_4$Sb$_3$ in TEGs, and the reason for this is still unknown. In addition, all previous study was only carried out using indirect experiment *e.g.* TE properties or in-situ powder X-ray diffraction in certain temperature or small (less than 10 K for Seebeck measurement) temperature gradient conditions [11,21–26]. In fact, pressed pellet TE element operates under conditions of power generating and large temperature gradients in TEG. Therefore, a new method is needed to develop to understanding the dynamic behavior of TE materials under operating conditions.

In our work, the operando study of Mg-doped β-Zn$_4$Sb$_3$ system under mimicking device condition is carried out using an advanced output power generation characteristics coupled with *in-situ* transmission electron microscopy (TEM). Mg doped β-Zn$_4$Sb$_3$ is known to have superior properties to undoped sample [22] and the present samples were developed with the aim of potential implementation in a commercial TEG. The TE properties were measured under conventional thermal cycling in helium atmosphere between room temperature and 718 K, while the power generating characteristics of the leg were investigated in an Argon atmosphere for an extended period of time under TEG working condition with hot and cold sides at 673 K and 293 K, respectively. The evolution of the microstructure was captured by *in-situ* TEM as temperature increased from 300 K up to 573 K. The crystalline structure was then determined from selected area diffraction (SAD) in connection with the high-resolution observation of atomic scale particle morphologies in the different temperature ranges to monitor the changes in the β-Zn$_4$Sb$_3$ sample.

2. Results

2.1. Thermoelectric properties of β-Zn$_4$Sb$_3$ under thermal cycling

Figure 1 shows the TE properties of doped $Zn_{3.96}Mg_{0.04}Sb_3$ (β-Zn_4Sb_3) between 300 K and 718 K up to 30 thermal cycles in ~0.1 MPa He gas. As seen in Figure 1, the electrical resistivity as a function of temperature exhibits a bell-shaped curve, which indicates a metallic conducting behavior in the temperature range from 300 K to 520 K and a semiconducting behavior in the temperature range of 520 K and 718 K both on heating and cooling. Interestingly, the electrical resistivity curve measured on heating and cooling exhibits a hysteresis loop in the temperature region of 450 and 650 K, where the value of the electrical resistivity is higher for the cooling curve than for the heating curve (Fig. 1a). In addition, in the vicinity of 520 K the change of the electrical resistivity curve is rather sharp and may be associated with a phase transition (this will be discussed in detail later in the discussion part).
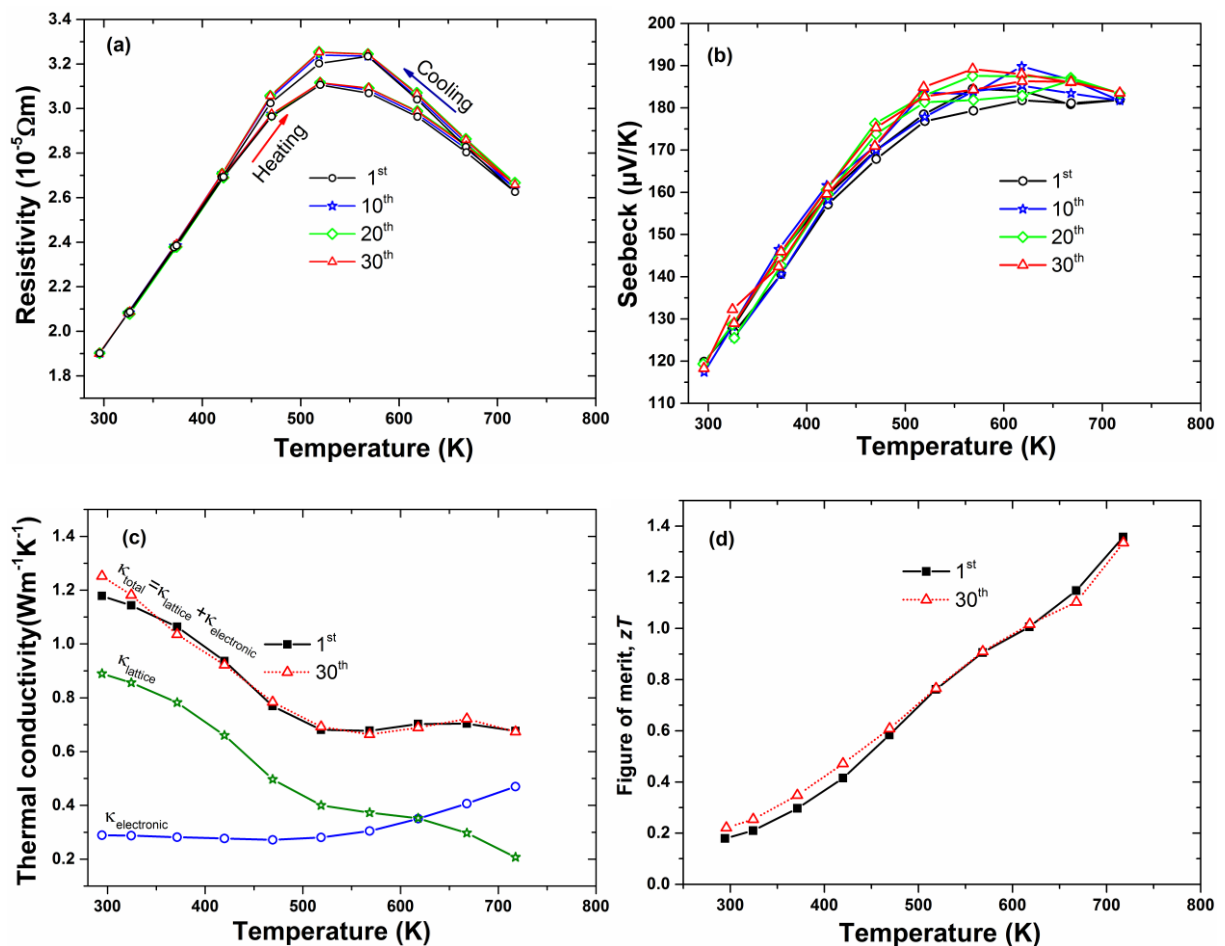

Figure 1 Thermal cycling measurement of the temperature dependence of: a) electrical resistivity, b) Seebeck coefficient, c) thermal conductivity and d) figure-of-merit.

The Seebeck coefficient has a positive value over the whole measured temperature range, indicating p-type behaviour of the sample, and the magnitude increases with increasing temperature from 120 µV/K at room temperature to a maximum of 185 µV/K at 500 K. During thermal cycling, the Seebeck coefficient appears to be relatively stable and the data scatter within the 8% uncertainty[30]. The change in power factor ($\alpha^2\sigma$), which is the combination of the electrical conductivity and the Seebeck coefficient, is minor after the 30th thermal cycle indicating high reproducibility and stability during the measurements (see Figure S1 supporting information). Fig. 1c shows the total measured thermal conductivity (κ_{total}) as a function of temperature taken on the 1st and 30th thermal cycles. The total thermal conductivity, $\kappa_{total} = \kappa_{electronic} + \kappa_{lattice}$ was calculated from the measurement of thermal diffusivity, γ, the heat capacity, C_p, and the density, D, by using the formula: $\kappa_{total} = D \times \gamma \times C_p$, while $\kappa_{electronic}$ was calculated using the Wiedemann-Franz relation. The Lorenz number can be calculated using the equation proposed by Kim et al.[31] $L = 1.5 + exp[-|\alpha|/116]$, which is more appropriate for thermoelectric materials. It is clear from Fig. 1c that the total thermal conductivity decreases sharply in the temperature range from 300 K to 520 K, and then it tends to saturate in the temperature range between 520 K and 718 K. The lattice thermal conductivity ($\kappa_{lattice}$) and the electronic thermal conductivity ($\kappa_{electronic}$) as a function of temperature are also plotted in Fig. 1c. In the temperature range between 300 K to 500 K, the thermal conductivity lattice component rapidly decreases while the electronic component is almost unchanged in the low-temperature range and slightly increases at elevated temperature. Fig.1d shows the material figure of merit, zT, as a function of temperature at the 1st and 30th thermal cycles. The zT values increase with increasing temperature from 0.2 at room temperature to 1.4 at 718 K. These zT values are among the highest values reported so far on Zn-Sb based materials [11,24]. Since the doping amount of Mg on Zn-sites is very small, the TE properties are slightly changed as compared with the pristine β-Zn_4Sb_3 [11]. However, it was

reported that the Mg-doped sample is more stable than the un-doped one [22]. These results revealed that the TE performance of β-Zn$_4$Sb$_3$ is maintained under thermal cycling in a helium atmosphere.

2.2. Dynamic behavior of β-Zn$_4$Sb$_3$ under large temperature gradient

In practical application, a TEG must be subjected to a large temperature gradient, which is maintained between a heat source and a heat sink. Under such conditions, the dynamic behavior of the materials plays a crucial role in the performance and the stability of TEG. In these investigations, β-Zn$_4$Sb$_3$ legs were tested under a large temperature gradient for a long period of time, while acquiring the current and voltage characteristics [32].

Figure 2 shows SEM images of a β-Zn$_4$Sb$_3$ leg 0 h and after 30 h subjecting the sample to large temperature gradient of 380 K created between 673 K and 293 K for 30 h. From this figure it is clearly seen that zinc whiskers (green color) grew on the cold side surface of the leg (Fig. 2b2). The general observations are that the Zn whisker concentration is much larger on the cold side than the hot side of the leg, the mechanism of whisker will be presented in discussion section. Within the legs (Fig. 2c-d), we found clear channels of pure Zn metal, which were confirmed by X-ray energy dispersive spectroscopy (EDS) analysis.
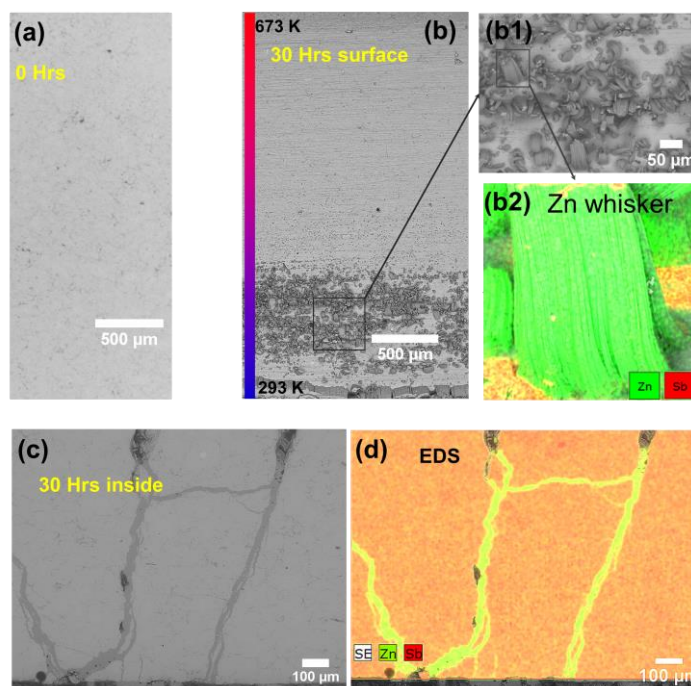
Figure 2. SEM micrographs of β-Zn_4Sb_3 leg 0 h (a) and after 30 h applying the large temperature gradient of 380 K with the hot side at 673 K and the cold side at 293 K (b-d).

2.3. Microstructure evolution

To understand the primary factors acting on the high-performance TE β-Zn_4Sb_3 material as well as its stability, *in-situ* transmission electron microscopy (TEM) investigation was carried out. Figure 3a-d presents a series of *in-situ* TEM micrographs showing the microstructure evolution in the β-Zn_4Sb_3. As temperature increases from 373 K to 573 K, nano-sized particles appears (Fig. 3a-d), and their concentration and size increase with increasing temperature (Fig. 3b1-d1). The average size of these nanoparticles is increasing from 12 nm at 373 K to 32 nm at 573 K. Previous studies identified these "nanoparticles" as nanoinclusions [17,26,33], and further analysis shown later in this work also identify such nanoinclusions as a nanoprecipitated phase on the matrix of primary structure.
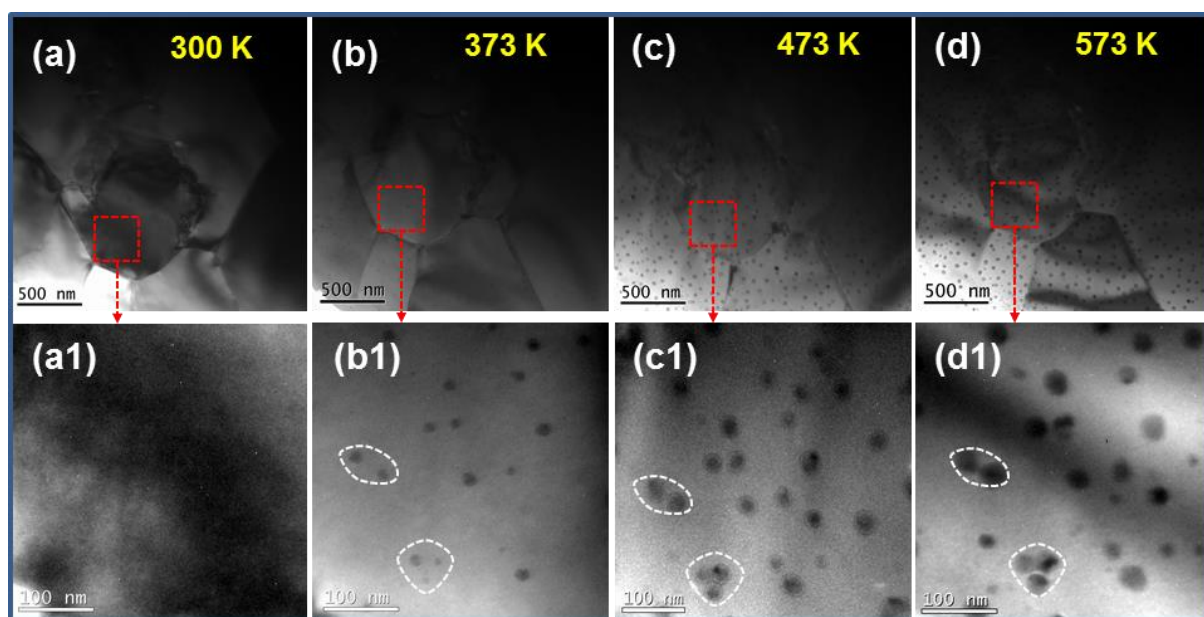

Figure 3 In-situ TEM study of microstructural evolution in β-Zn_4Sb_3 sample: (a-d) BF-TEM images recorded at various temperatures, (a1-d1) magnified BF-TEM images from selected area on the specimen for better visibility of nanostructural evolution.

Figure 4 shows selected-area electron diffraction (SAD) patterns at 300 K and 573 K. A well-defined spot pattern of the single phase rhombohedral structure is visible in the sample at 300 K with the lattice constants of *a* = *b* = 1.230 nm and *c* = 1.248 nm (details of this structure are presented in supporting information, Fig. S2 and Fig. S3).
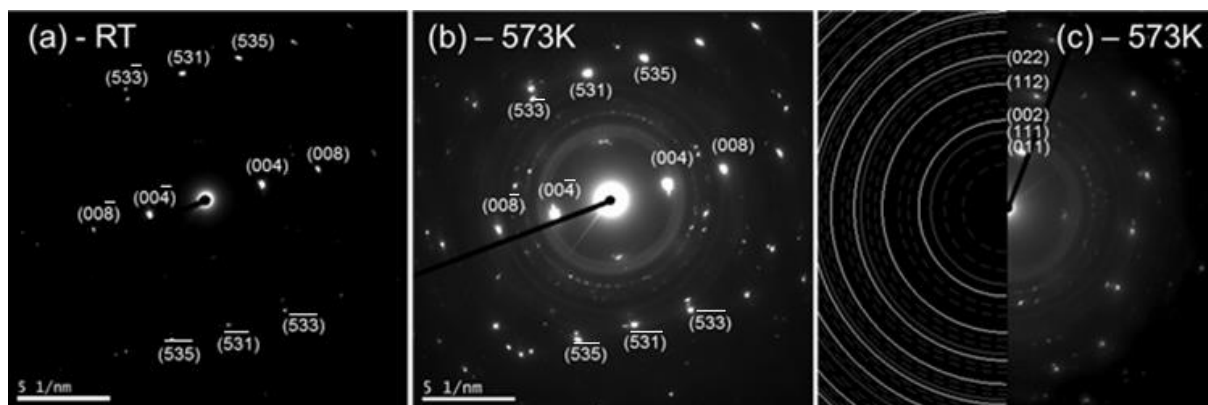
8

Figure 4 SAD patterns obtained from BF-images in the *in-situ* heating experiment (Fig. 3): (a) SAD pattern at 300 K, (b) SAD pattern at 573 K and (c) ring pattern in (b) fitted with theoretical ring pattern of the standard structure.

Indexing the ring pattern [34] in Fig. 4c reveals a trigonal/hexagonal unit cell of the secondary phase (space group $R\bar{3}c$) with lattice constants of a = 1.235 nm, b = 0.775 nm, c = 1.251 nm (about 4% uncertainty). This result suggests that structure of the secondary phase is distorted from the primary rhombohedral structure.

To identify the composition of these nanoinclusions, elemental mapping was conducted using high angle annular dark field scanning transmission electron microscopy (HAADF-STEM) imaging and EDS mapping and the results are shown in Fig. 5.
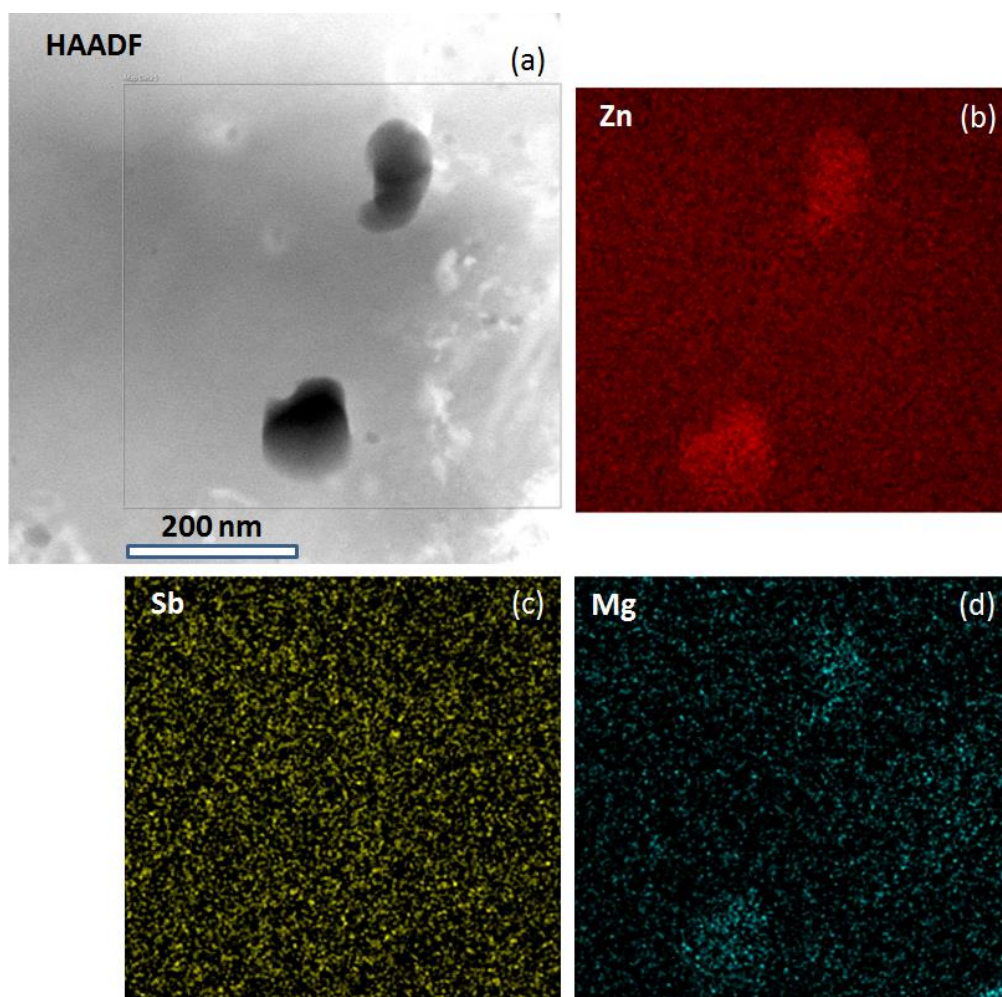
Figure 5 (a) HAADF-STEM image of the β-Zn$_4$Sb$_3$ at 573 K showing two nano-precipitated dots formed in the primary phase, (c-d) EDS elemental maps of Zn, Sb and Mg obtained from a marked area in the HAADF image.

Enrichment of Zn and Mg in the nanoinclusions phase grown in the β-Zn$_4$Sb$_3$ matrix at high temperature can be clearly observed from the EDS elemental maps (Fig. 5b-d) where a stronger contrast of Zn and Mg is observed in the map. Higher concentration of Zn and Mg in the nanoinclusion regions causes a darker contrast as visibly seen the STEM-HAADF image (Fig. 5a). In contrast, the concentration of Sb seems almost unchanged from the matrix of the primary phase to the precipitated phase.

3. Discussions

The bell-shaped behavior in the electrical resistivity as a function of temperature on heating and cooling could be associated with the inverse solubility of Zn from the main β-Zn$_4$Sb$_3$ matrix into the Zn-rich phase nanoparticle. According to calculations in Ref. [35], the

precipitation and the reabsorption of Zn will occur when the β-Zn_4Sb_3 sample is heated up from 300 K to 718 K. In the first process, as the temperature increases from 300 K to 520 K interstitial Zn starts to migrate and precipitate forming various secondary-phase nanoinclusions (showing a ring pattern in Fig. 4b) leading to an increase in the electrical resistivity. As the temperature increases above 520 K, the Zn precipitation becomes saturated, and reabsorption of Zn back to the matrix starts occurring. The electrical resistivity thereby starts decreasing with further increasing temperature. During cooling, due to thermodynamic equilibrium similar absorption and precipitation also occur [35]. Together with the structural analysis (Fig. 4), it can be concluded that the migration of Zn has caused a structure distortion resulting in the sharp change of the electrical resistivity curve (Fig. 1a). This could also be the reason on cooling the electrical resistivity has shown the hysteresis loop in the temperature region of 450 and 650 K, as shown in Fig. 1a.

As shown in Figure 1d, the high zT value of the β-Zn_4Sb_3 sample is mainly due to the low thermal conductivity and the low electrical resistivity. The source of these effects can be clarified from the formation of the sample microstructure. Firstly, the microstructural evolution can explain the origin of the extremely low thermal conductivity owing to the formation of Zn-rich nano-sized particles in the main matrix at an elevated temperature which strongly suppresses the lattice thermal conductivity component, as shown in Fig. 1c. The reduction in the thermal conductivity seems to be proportional to the concentration of Zn-rich nanoinclusions in the temperature range of 300 K and 520 K. Secondly, TEM observation at room temperature (in Figure S2b supporting information) shows contrast (dark fringes) of misfit dislocations in the sample which could be further reason for the reduction of the thermal conductivity (Fig. 1c). The existence of misfit dislocations in Zn-Sb alloys seems to be an intrinsic property resulting from the high mobility and non-stoichiometry of Zn atoms acting as self-insertions[36]. A high density of misfit dislocation was found previously to play a

major role in the reduction of the thermal conductivity due to intrinsic phonon scattering [36,37]. In addition, it allows a path for the charge carriers to transport with a low resistance. Thus, the low thermal conductivity and low electrical resistivity combine with the high Seebeck coefficient have led to achieve the high zT value of 1.4 at 718 K for the β-Zn_4Sb_3 sample, as clearly shown in Fig. 1d.

It should be noted that the formation of a nanostructured secondary phase during heating in the β-Zn_4Sb_3 alloys has been previously suggested due to the decomposition [21–26,38]. However, our *in-situ* TEM observation and structural analysis revealed that there is no decomposition process occurring over the whole investigated temperature region from 300 K to 718 K. On the other hand, by looking closer to the secondary phase shown in magnified BF TEM images in Fig. 3d1 and in HRTEM images (in Figure S4, supporting information), the grain boundary between the primary and the secondary phase is very difficult to be identified. The lattice constants of the secondary phase indicate that the secondary phase is distorted from the mother phase of the matrix due to symmetry breaking [39] rather than a separate granular phase. This suggests that the precipitation of the secondary nanoinclusion phase is caused by the migration Zn and Mg atoms into the misfit dislocations. Such a phase distortion by the migration of Zn into misfit dislocations was also observed in some Zn alloys including Zn-Sb system [40–43].

When the β-Zn_4Sb_3 leg is placed under a large temperature gradient, those mobile Zn from the nano-precipitated Zn-rich phase will precipitate on the cold side of the leg[35]. When operating under large temperature gradient for an extended period of time (e.g. 30 h), Zn whiskers keep growing towards the surface of the sample (Fig. 2b) and as a result continuous Zn micro-channels are formed inside the leg (Fig. 2c). On the cold side of the leg, due to a higher cooling power the precipitation is highly expedited, and as a consequence, the whiskers tend to grow faster, as clearly seen in Fig. 2b. The precipitation of Zn from β-Zn_4Sb_3 results in

a change in the volume of the sample leading to sample cracking, and in some cases, the effect even leads to breaking of the glass ampoule [35]. As the Zn whiskers continuously grow and cracks in the sample occur, the open circuit voltage unremittingly increases during the 30h test (see Figure S5b). Therefore, in order to use β-Zn_4Sb_3 in a practical TEG application the migration/precipitation of Zn interstitial site should be isolated by e.g. making a core-shell or layer by layer in functionally graded material structures where each single core or a single layer of β-Zn_4Sb_3 is worked under a small temperature gradient.

3. Conclusion

We have investigated the high-performance thermoelectric $Zn_{3.96}Mg_{0.04}Sb_3$ under large temperature gradients and thermal cycling in a helium atmosphere. The results have confirmed that the *zT* values are maintained with a maximum value up to 1.4 at 718 K after 30 thermal cycles. The origin of the extremely low thermal conductivity was found to be due to the formation of Zn-rich nanoparticles in the matrix, and the concentration of nano-inclusions increased with increasing heating temperature as clearly observed by *in-situ* TEM analysis. However, under the temperature gradient of 380 K for 30 hours, gradual precipitation of zinc whiskers on the cold side of the β-Zn_4Sb_3 leg was observed. The microstructural evolution observed by in-situ TEM has revealed the migration of Zn, which is the main driving force for the dynamic behavior of $Zn_{3.96}Mg_{0.04}Sb_3$ under thermal cycling and large temperature gradient. In-situ TEM analysis also pointed out that there is no decomposition of the $Zn_{3.96}Mg_{0.04}Sb_3$ sample in the temperature range of 300 K to 573 K. These findings provide a deep understanding the dynamic behavior of β-Zn_4Sb_3. The operando study method in present studies also provides a useful tool to understand and develop future high performance and stable TE materials and devices.

4. Experimental Section

Sample Fabrication:

99.99% zinc shots, 99.5% antimony powder, and 99% Mg shots were weighed according to the stoichiometry of $Zn_{3.96}Mg_{0.04}Sb_3$ and sealed in quartz ampoule after evacuation to 10^{-4} Pa and flushing Argon gas for at least three times. The ampoules were placed horizontally in a tube furnace and heated to 973 K with a heating rate of 400 K/h under continuous rotation, which helps homogenizing the melt. The samples were held at this temperature for 2 h before quenching with ice water. The resulting polycrystalline solids were ground and sieved (<45 μm). The powder was then compacted by Spark Plasma Sintering (SPS) into half-inch disks with a thickness of ~3 mm.

Seebeck Coefficient and Resistivity Measurements:

The Seebeck coefficient and the electrical resistivity were simultaneously performed using the commercial equipment Ulvac-Riko Zem-3 from room temperature up to 718 K under helium pressure of 0.1 Bar. The thermal conductivity (κ) was calculated from the measured thermal diffusivity (γ), the mass density (δ), and the specific heat capacity (C_p) in relation to the equation $\kappa = \gamma \times D \times C_p$. The thermal diffusivity was acquired by the laser flash method (Netzsch LFA-457, Germany), the mass densities of the samples were measured by Archimedes' method using water with surfactant, and the specific heat capacity was obtained by using a differential scanning calorimeter (Netzsch DSC 404C, Germany).

Large temperature gradient characterization:

The measurement of power generation characteristics of the single β-Zn_4Sb_3 leg was performed in air using an in-house Rig-test system. The voltage of the leg was directly measured while the electric current was calculated from the dropped voltage on the shunt resistance with the external electrical load. The control software system is based on Apache web server software (Open Source Software, OSS) and allows flexibility with regard to the type gas control, cycling, long-term stability tests, etc. In order to define an accurate temperature difference

across the leg, 0.5mm N-type thermocouple was directly inserted inside the Ag electrodes in the vicinity of the top part of the leg. The thermocouple at the hot side was also used for setting up the PID of the heater controller. The detail of the experimental set up may be seen elsewhere [32,44].

Electron Microscopy Analyses:

The microstructure of the thermoelectric legs before and after test under large temperature gradient was observed by scanning electron microscope (SEM) TM3000.

Microstructure and crystal structure of the material were studied by means of transmission electron microscopy (TEM) and selected area electron diffraction (SAD) in TEM combined with *in-situ* heating experiment using a Jeol JEM 3000F equipped with a field emission gun (FEG) operating at an accelerated voltage of 300 kV, and a FEI Tecnai F30 (300 kV, FEG) equipped with high angle annular dark field (HAADF) dectector and silicon drift detector (SDD) for X-ray energy dispersive spectroscopy (EDS). TEM specimens were prepared by Ar ion milling, and *in-situ* heating experiment in TEM was performed on a Gatan heating holder.

References

[1]   G. J. Snyder, M. Christensen, E. Nishibori, T. Caillat, B. B. Iversen, *Nat. Mater.* **2004**, *3*, 458.

[2]   G. Slack, In *CRC Handbook of Thermoelectrics*; CRC Press, 1995.

[3]   L. T. Hung, N. Van Nong, S. Linderoth, N. Pryds, *Phys. status solidi* **2015**, *212*, 767.

[4]   G. J. Snyder, E. S. Toberer, *Nat. Mater.* **2008**, *7*, 105.

[5]   L.-D. Zhao, S.-H. Lo, Y. Zhang, H. Sun, G. Tan, C. Uher, C. Wolverton, V. P. Dravid, M. G. Kanatzidis, *Nature* **2014**, *508*, 373.

[6]   C. Fu, S. Bai, Y. Liu, Y. Tang, L. Chen, X. Zhao, T. Zhu, *Nat. Commun.* **2015**, *6*, 8144.

[7]   G. Rogl, A. Grytsiv, K. Yubuta, S. Puchegger, E. Bauer, C. Raju, R. C. Mallik, P. Rogl, *Acta Mater.* **2015**, *95*, 201.

[8]   K. Biswas, J. He, I. D. Blum, C.-I. Wu, T. P. Hogan, D. N. Seidman, V. P. Dravid, M. G. Kanatzidis, *Nature* **2012**, *489*, 414.

[9]   H. Liu, X. Shi, F. Xu, L. Zhang, W. Zhang, L. Chen, Q. Li, C. Uher, T. Day, G. J. Snyder, *Nat. Mater.* **2012**, *11*, 422.

[10]   Y. Sun, M. Christensen, S. Johnsen, N. V. Nong, Y. Ma, M. Sillassen, E. Zhang, A. E. C. Palmqvist, J. Bøttiger, B. B. Iversen, *Adv. Mater.* **2012**, *24*, 1693.

[11]   T. Caillat, J.-P. Fleurial, A. Borshchevsky, *J. Phys. Chem. Solids* **1997**, *58*, 1119.

[12]   B. B. Iversen, *J. Mater. Chem.* **2010**, *20*, 10778.

[13]   H. W. Mayer, I. Mikhail, K. Schubert, *J. Less Common Met.* **1978**, *59*, 43.

[14]   Y. Mozharivskyj, A. O. Pecharsky, S. Bud'ko, G. J. Miller, *Chem. Mater.* **2004**, *16*, 1580.

[15]   F. Cargnoni, E. Nishibori, P. Rabiller, L. Bertini, G. J. Snyder, M. Christensen, C. Gatti, B. B. Iversen, *Chem. - A Eur. J.* **2004**, *10*, 3861.

[16]   H. J. Kim, E. S. Božin, S. M. Haile, G. J. Snyder, S. J. L. Billinge, *Phys. Rev. B* **2007**, *75*, 134103.

[17]   Ø. Prytz, a. E. Gunnæs, O. B. Karlsen, T. H. Breivik, E. S. Toberer, G. Jeffrey Snyder, J. Taftø, *Philos. Mag. Lett.* **2009**, *89*, 362.

[18]   E. S. Toberer, K. a. Sasaki, C. R. I. Chisholm, S. M. Haile, W. a. Goddard, G. J. Snyder, *Phys. status solidi – Rapid Res. Lett.* **2007**, *1*, 253.

[19]   J. Nylén, M. Andersson, S. Lidin, U. Häussermann, *J. Am. Chem. Soc.* **2004**, *126*, 16306.

[20]   B. B. Iversen, *J. Mater. Chem.* **2010**, *20*, 10778.

[21]   Y. Mozharivskyj, Y. Janssen, J. L. Harringa, A. Kracher, A. O. Tsokol, G. J. Miller, *Chem. Mater.* **2006**, *18*, 822.

[22]   H. Yin, B. B. Iversen, *Sci. Adv. Mater.* **2011**, *3*, 592.

[23]   H. Yin, M. Christensen, B. L. Pedersen, E. Nishibori, S. Aoyagi, B. B. Iversen, *J. Electron. Mater.* **2009**, *39*, 1957.

[24]   B. L. Pedersen, H. Yin, H. Birkedal, M. Nygren, B. B. Iversen, *Chem. Mater.* **2010**, *22*, 2375.

[25] S. Y. Wang, X. Y. She, G. Zheng, F. Fu, H. Li, X. F. Tang, *J. Electron. Mater.* **2012**, *41*, 1091.

[26] H. Yin, S. Johnsen, K. A. Borup, K. Kato, M. Takata, B. B. Iversen, *Chem. Commun.* **2013**, *49*, 6540.

[27] T. Dasgupta, C. Stiewe, A. Sesselmann, H. Yin, B. B. Iversen, E. Mueller, *J. Appl. Phys.* **2013**, *113*, 103708.

[28] T. Dasgupta, C. Stiewe, L. Boettcher, H. Yin, B. B. Iversen, E. Mueller, *MRS Proc.* **2011**, *1325*, mrss11.

[29] S. Wang, H. Li, D. Qi, W. Xie, X. Tang, *Acta Mater.* **2011**, *59*, 4805.

[30] H. Wang, S. Bai, L. Chen, A. Cuenat, G. Joshi, H. Kleinke, J. König, H. W. Lee, J. Martin, M.-W. Oh, W. D. Porter, Z. Ren, J. Salvador, J. Sharp, P. Taylor, A. J. Thompson, Y. C. Tseng, *J. Electron. Mater.* **2015**, *44*, 4482.

[31] H.-S. Kim, Z. M. Gibbs, Y. Tang, H. Wang, G. J. Snyder, *APL Mater.* **2015**, *3*, 41506.

[32] L. T. Hung, N. Van Nong, G. J. Snyder, M. H. Viet, B. Balke, L. Han, E. Stamate, S. Linderoth, N. Pryds, *Energy Convers. Manag.* **2015**, *99*, 20.

[33] T. Zou, X. Qin, Y. Zhang, X. Li, Z. Zeng, D. Li, J. Zhang, H. Xin, W. Xie, A. Weidenkaff, *Sci. Rep.* **2015**, *5*, 17803.

[34] M. Klinger, A. Jager, *J. Appl. Crystallogr.* **2015**, *48*, 2012.

[35] G. S. Pomrehn, E. S. Toberer, G. J. Snyder, A. van de Walle, *Phys. Rev. B* **2011**, *83*, 94106.

[36] P. Rauwel, O. M. Løvvik, E. Rauwel, E. S. Toberer, G. J. Snyder, J. Taftø, *Phys. status solidi* **2011**, *208*, 1652.

[37] N. Peranio, O. Eibl, J. Nurnus, *J. Appl. Phys.* **2006**, *100*, 114306.

[38] J. Lin, X. Li, G. Qiao, Z. Wang, J. Carrete, Y. Ren, L. Ma, Y. Fei, B. Yang, L. Lei, J. Li, *J. Am. Chem. Soc.* **2014**, *136*, 1497.

[39] W. Liu, X. Yan, G. Chen, Z. Ren, *Nano Energy* **2012**, *1*, 42.

[40] E. Hawbolt, T. Massalski, *Metall. Trans.* **1970**, *1*, 2315.

[41] M. Werner, H. Löffler, *Cryst. Res. Technol.* **1983**, *18*, 459.

[42] P. M. Jardim, G. Solórzano, J. B. V Sande, *Mater. Sci. Eng. A* **2004**, *381*, 196.

[43] A. Faghaninia, C. S. Lo, *J. Phys. Condens. Matter* **2015**, *27*, 125502.

[44] L. T. Hung, N. Van Nong, L. Han, R. Bjørk, P. H. Ngan, T. C. Holgate, B. Balke, G. J. Snyder, S. Linderoth, N. Pryds, *Energy Technol.* **2015**, *3*, 1143.